Enhanced visible-light-driven photocatalytic activity of mesoporous TiO$_{2-x}$N$_x$ derived from the ethylenediamine-based complex

Zheng Jiang,*[ab] Liang Kong,[a] Feraih Sh. Alenazey,[c] Yangdong Qian,[a] Liam France,[a] Tiancun Xiao[a] and Peter P. Edwards*[a]

A facile solvent evaporation induced self-assembly (SEISA) strategy was developed to synthesize mesoporous N-doped anatase TiO$_2$ (SE-meso-TON) using a single organic complex precursor derived *in situ* from titanium butoxide and ethylenediamine in ethanol solution. After the evaporation of ethanol in a fume hood and subsequent calcinations at 450 °C, the obtained N-doped TiO$_2$ (meso-TON) anatase was of finite crystallite size, developed porosity, large surface area (101 m^2 g^{-1}) and extended light absorption in the visible region. This SE-meso-TON also showed superior photocatalytic activity to the SG-meso-TON anatase prepared *via* sol–gel synthesis. On the basis of characterization results from XRD, XPS, N$_2$ adsorption–desorption and ESR, the enhanced visible-light-responsive photocatalytic activity of SE-meso-TON was assigned to its developed mesoporosity and reduced oxygen vacancies.

Introduction

Motivated by the discovery of the excellent visible-light-response of nitrogen-doped TiO$_2$ (TiO$_{2-x}$N$_x$, hereafter, TON),[1,2] various nonmetal dopants (*e.g.* N, C, S, P, and halogen elements) have been extensively attempted to be doped or co-doped into the TiO$_2$ matrix for narrowing its wide bandgap (∼3.2 eV) and thus harvesting visible light.[3] Among those doped TiO$_2$ materials, TON is more desirable due to its low energy requirement for doping and superb performance in photovoltaic and photocatalytic applications.[2,4–7] In practice, the mesoporous TON (meso-TON) is plausible because its large specific surface area (SSA) and developed porosity favour solar energy conversion.[4,8] Despite the fact that enormous advances have been achieved in the control of N-doping level, morphology, crystallite size and crystallinity of TiO$_{2-x}$N$_x$,[9–11] synthesis of mesoporous TiO$_{2-x}$N$_x$ (meso-TON) remains a great challenge because the mesoporous structure is prone to collapse during nitriding and crystallization at elevated temperature.[8,12–14]

Ammonolysis is the most used nitriding technique for preparation of TON, though it occurs above 500 °C.[2,10,13] Such a high ammonolysis temperature inevitably destructs the porosity of the primitive meso-TiO$_2$, induces phase transition

and hampers its applications in thin film devices.[2,10] In order to retain its developed porosity, a few low-temperature methodologies, such as sol–gel,[9] hydrothermal or solvothermal combined with post-nitriding,[10,11] have been developed for preparing meso-TON. In those methodologies, the involved solvent, surfactant template and chemical sources of Ti and N controlled the hydrolysis, nitriding and crystallization processes and thus determined the mesoporosity of the resultant TON.[15,16] In particular, the alternative nitrogen sources to NH$_3$, such as NH$_4$Cl,[13] urea,[15,17,18] HMT,[19] glycine[16] and thiourea,[20] are plausible for realizing low-temperature nitriding.

Solvent evaporation induced assembly (SEISA) has been demonstrated to be an excellent route to prepare meso-TiO$_2$ thin films,[12] in terms of its great flexibility in handling the synthesis system (solvents, surfactant templates and precursors). Moreover, with dedicated design and operation, the evaporated solvent may be recycled, marking it an environmental-friendly synthesis route to scale up. SEISA was successful in preparation of meso-TON thin films *via* post-nitriding meso-TiO$_2$ photoelectrodes,[4,12] but it has not yet succeeded in synthesis of meso-TON powders. Given a suitable nitrogen source employed with a volatile solvent under controlled hydrolysis of a titanium precursor, it is highly possible to prepare meso-TON nanocrystals through SEISA synthesis.

We here report a simple SEISA methodology to synthesize mesoporous TON crystallites, in which a novel titanium complex derived *in situ* from titanium butoxide and ethylenediamine (EDA) acted as a single precursor,[21] ethanol the volatile solvent and dodecylamine (DDA) the surfactant template. The meso-TON synthesized *via* SEISA showed

[a] *Inorganic Chemistry Laboratory, University of Oxford, Oxford, OX1 3QR, UK. E-mail: zhjiang76@hotmail.com; peter.edwards@chem.ox.ac.uk; Fax: +44 (0)1865 272656; Tel: +44 (0)1865 272660; +44 (0)1865-272646*

[b] *Environment Sustainability Institute, University of Exeter, Cornwall Campus, Penryn, Cornwall, TR10, 9EZ, UK*

[c] *Energy Research Institute, King Abdulaziz City for Science and Technology, Riyadh, Saudi Arabia*

developed mesoporosity and high photocatalytic activity under visible-light irradiation. On the basis of key characterizations, we proposed the synthesis mechanism and the nature of the N-dopant.

Experimental section

Chemicals

Dodecylamine (DDA, 98% Alfa Aesar), ethylenediamine (EDA, 99% Alfa Aesar), titanium butoxide (Ti(t-OBu)$_4$, 98% Alfa Aesar) and absolute ethanol were purchased from Aldrich, and used without further treatment.

Synthesis

The SE-meso-TON was prepared through ethanol evaporation induced assembly of the as-formed Ti–N complex and DDA was used as the template to form the mesoporous structure, in which the Ti(t-OBu)$_4$/EDA/DDA molar ratio is 4 : 2 : 1. Briefly, 2.5 mmol DDA and 10 mmol Ti(OBu)$_4$ were dissolved into 15 mL ethanol, followed by the dropwise addition of 5.0 mL ethanol solution containing 0.6 g EDA under vigorous stirring. The resulting yellow solution was continuously stirred at room temperature for 3 hours before placing in the fume hood overnight to evaporate the solvent. In order to remove the template and crystallize TON, the resultant dry gel was calcined at 350 °C for 4 hours, and the received black sample was calcined further at 450 °C for 4 hours. The heating rate is 1 °C min^{-1} in a muffle furnace under stationary air. The obtained TON is denoted as SE-meso-TON, where meso is the abbreviation of mesoporous and SE denotes the SEISA method. For comparison, SG-meso-TON was synthesized *via* a sol–gel method in a quite similar process to SE-meso-TON except for adding 2 g distilled water to the EDA, DDA and ethanol mixture.

Characterization techniques

Low-angle (0.5–10°) and wide-angle X-ray powder diffraction (XRD) patterns were performed on a X'Pert, PANALS diffractometer, using Cu Kα1 radiation (40 kV, 40 mA). The crystallite size of the meso-TON materials was calculated using the Scherrer equation. High-resolution transmission electron microscopy (HRTEM) images were taken through a JEOL 3000F electron microscope. The samples were dispersed into ethanol prior to deposition on carbon–copper grids for HRTEM characterizations. Nitrogen adsorption isotherms were obtained at 77 K on a Micromeritics ASAP 2020 after degassing the samples at 300 °C for 3 h. Brunauer–Emmett–Teller (BET) surface areas were calculated from the linear part of the BET plot. Pore-size distributions were calculated using the Barrett–Joyner–Halenda (BJH) model with Halsey equation.

The UV-vis spectra of the N-doped TiO$_2$ sample in the 260–800 nm range were recorded using a Perkin-Elmer Lambda 35 UV-vis spectrophotometer equipped with an integrating sphere, and BaSO$_4$ was used as the reference. The surface property of the TON samples was characterized by X-ray photoelectron spectroscopy (XPS) on a Perkin-Elmer PHI 1600 ESCA system with a monochromatic Mg Kα source and a charge neutralizer. Shirley

backgrounds were applied when fitting the XPS peaks. The electron spin resonance (ESR) spectra were recorded on a Magnettech Miniscope MS200 EMX spectrometer operating at room temperature, 100 kHz magnetic field modulation, a fixed microwave frequency of 98.66 GHz and power attenuation 15 dB.

Photocatalysis experiments

The photocatalytic activities of the meso-TON samples and commercial P25 TiO$_2$ (Degussa TiO$_2$ aerosol) were evaluated by decomposing RhB under visible-light irradiation. The optical system used for the photocatalytic reaction consisted of an overhead 300 W xenon lamp (PLS-SXE 300, Beijing TrustTech) equipped with both UV and IR cut-off filters (UVCUT 400 and IR filter, Beijing TrustTech), which were attached to the lamp source to completely remove all incoming wavelengths shorter than 390 nm and greater than 800 nm to ensure irradiation with visible light only. The light intensity was measured and remained at 50 mW cm^{-2} for each test. In each experiment, reaction suspension was prepared by adding 0.1 g photocatalyst into a 100 mL aqueous solution of RhB (20 mg L^{-1}). Prior to irradiation, the suspensions were stirred in the dark for 1 hour to establish adsorption–desorption equilibrium of the dye on the catalysts' surfaces. During photo-reaction, approximately 3 mL of suspension was collected at certain intervals and then centrifuged (10 000 rpm, 4 min) to remove the photocatalyst particles. The collected supernatant solutions were analyzed by a Perkin-Elmer Lambda 750S UV-visible spectrometer. The characteristic absorption peak of RhB at 554 nm was used to determine the degradation extent of RhB.

Results and discussion

Fig. 1A shows the wide-angle XRD patterns of the SE-meso-TON and SG-meso-TON samples calcined at 450 °C. The Bragg diffraction data of the meso-TON samples can be well indexed to the anatase crystal phase (JCPDS: 84-1285).[22,23] The diffraction peak intensities of the SE-meso-TON sample are weaker than those of SG-meso-TON, suggesting that the SE-meso-TON has smaller crystallite size. As listed in Table 1, the crystallite size of SE-meso-TON is approximately 10 nm, two thirds of that of SG-meso-TON (15.6 nm), revealing that such SEISA is an effective route to prepare mesoporous nanocrystalline TON. In addition, there are only broad single diffraction peaks around 2° in the small-angle XRD patterns of these meso-TON samples (Fig. 1B), indicating that the materials possess disordered mesopores.[12] Similar low-angle XRD (SAXRD) patterns were previously observed on meso-TiO$_2$ synthesized *via* organic amine surfactant templates,[24-26] though the SAXRD peaks disappeared due to structure collapse above 300 °C. The stronger SAXRD pattern of SE-meso-TON suggests that it is more resistant to sintering than SG-meso-TON. The high thermal stability of SE-meso-TON promises its great potential for application in photocatalysis and dye sensitized solar cells.[5,12,27]

The TEM images in Fig. 2A and B clearly show that the SG-meso-TON and SE-meso-TON samples possess disordered mesopores, with a diameter of 2–6 nm and formed among
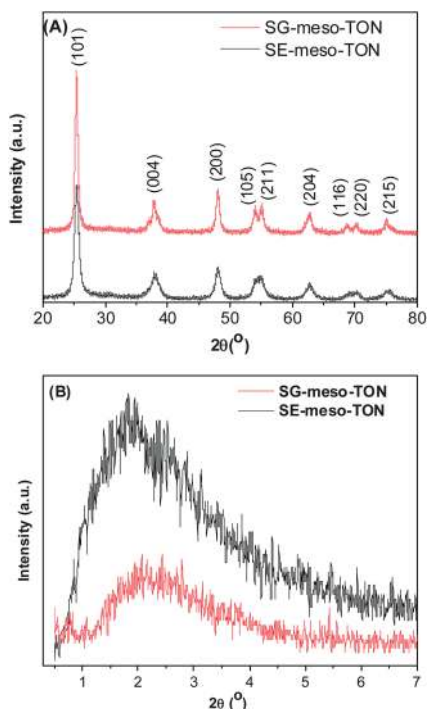
Fig. 1 (A) Wide-angle and (B) small-angle XRD patterns of the nanocrystalline meso-TON calcined at 450 °C.

Table 1 Physical and chemical properties of the meso-TON samples

Samples	Crystallite size (nm)	D_p (nm)	SSA (m^2 g^{-1})	E_g^a (eV)	k_{RhB}^b	TOF^c
SE-meso-TON	10.0	4.5	101	2.98	0.0701	0.0070
SG-meso-TON	15.6	3.5	55	2.90	0.0236	0.0043

[a] The bandgap energy, E_g, was derived from $E_g = 1239.8/\lambda_g$, where λ_g is the absorption edge in the UV-vis spectra. [b] The reaction kinetics constant derived from $-\ln(c/c_0)$ *vs.* time. [c] Turnover frequency (m^{-2} g^{-1} min^{-1}).

jointly aggregated nanoparticles. Besides the mesopores, micropores (diameter below 2 nm) can also be observed in the HRTEM image (Fig. 2C) on the individual SE-meso-TON particle, suggesting that it has hierarchical porous architecture. The sharp SAED concentric rings in the inset of Fig. 2B and the
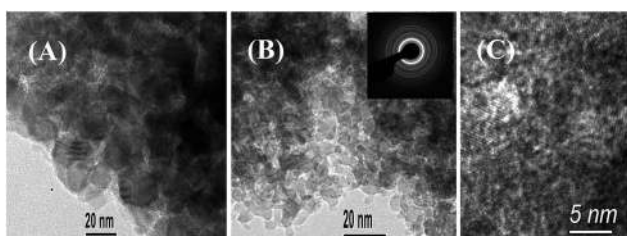

Fig. 2 TEM images of the SG-meso-TON (A) and SE-meso-TON (B) and an HRTEM image of SE-meso-TON (C) calcined at 450 °C. The inset in (B) is the selected area electron diffraction pattern (SAED) of SE-meso-TON.

lattice fringes in Fig. 2C indicate that the SE-meso-TON has well defined crystallites. Such hierarchical porous architecture of the nanocrystalline TON is highly desired in solar energy conversion.[5,6,12,24,25]

Fig. 3A shows the nitrogen adsorption–desorption isotherms of the SE-meso-TON and SG-meso-TON samples calcined at 450 °C. The type-IV isotherm curves of the samples further verified their mesoporous features.[28,29] Their H2 type hysteresis loops in the relative pressure (P/P_0) range of 0.4–0.8 suggest that the materials have ink-bottle-shaped pores. Fig. 3B presents the Barrett–Joyner–Halenda (BJH) pore size distribution profiles of the meso-TON, revealing that the meso-TON materials have similar pore size distributions but SE-meso-TON owns the larger mean pore size (4.5 nm). The BJH profiles below the 2 nm range indicate that SE-meso-TON has more micropores than SG-meso-TON. Ultrasonic synthesis was ever attempted to synthesize pure porous TiO_2 with very large SSA (over 600 m^2 g^{-1}) using a DDA template, though its SSA value dramatically reduced to 38 m^2 g^{-1} after being calcined at 350 °C because the original porous TiO_2 mainly consists of micropores and merged during thermal treatments.[24] It is also noted that the SSA of SE-meso-TON is 101 m^2 g^{-1} after calcination at 450 °C, nearly twice that of SG-meso-TON (55 m^2 g^{-1}). Such a large SSA of SE-meso-TON at 450 °C indicates that the synthesis methodology, in particular, the involvement of EDA and DDA, may retain the developed porosity during thermal crystallization.

In order to interpret the formation mechanism of the mesoporous TON in SEISA, we proposed a "coordination-hydrolysis-assembly" pathway. Firstly, EDA will attack and partially replace the butoxyl group in $Ti(OBu)_4$ to coordinate with Ti through Ti–N bonds, forming titanium–ethylenediamine complexes, $Ti_x(OBu)_{4x-y}(EDA)_{y/2}$, denoted as EDA–Ti.[21,30] Following ethanol
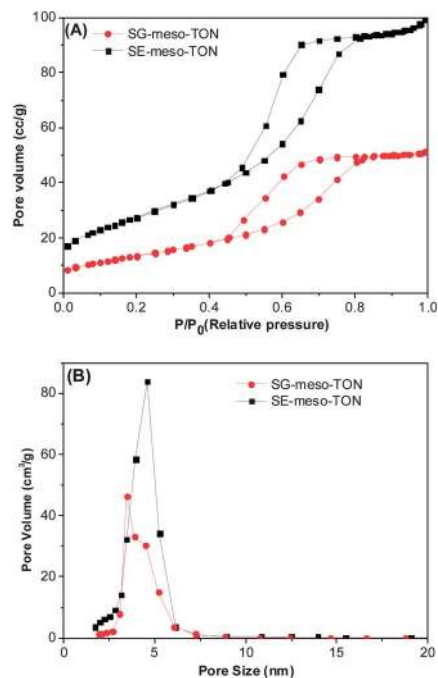
Fig. 3 N_2 adsorption–desorption isotherm (A) and pore size distribution (B) of the meso-TON samples calcined at 450 °C.

evaporation, the Ti–EDA would slowly hydrolyze to form a Ti_x $(EDA)_{y/2}(OH)_{4w-y}$ complex (denoted as EDA–Ti–OH). In addition, as an alkali, EDA can somehow catalyze the subsequent hydrolysis. Concurrently, the partially hydrolyzed complex will assemble alongside DDA templates via a hydrogen bond with OH groups of the EDA–Ti–OH complex. Using ^{15}N-NMR D. Antonelli[26] experimentally confirmed that the H-bond rather than the chemical bond between the Ti precursor and DDA in the DDA-directed synthesis of meso-TiO₂. Finally, the mesoporous N-doped TiO_2 architecture was generated during the calcinations of the hydrolyzed complex, in which the DDA template was removed thermally accompanying the decomposition of the EDA–Ti–OH complexes.

The pre-calcination treatments at 350 °C carbonized the surfactant and the Ti–EDA–OH complex to form granular carbon particles, which offered the samples a black colour. The in situ generated carbon particulates act as hard templates for the formation of the porous network of the meso-TON. The amount of the carbon templates generated in forming SE-meso-TON would differ from those of SG-meso-TON. Sol–gel synthesis usually involves a larger amount of water for hydrolysis of the molecule precursor than the SEISA process, which absorbs humid moisture from the air and thus an extremely slow hydrolysis.[18] The slower hydrolysis of the EDA–Ti precursor offers a prolonged time for the in situ as-formed EDA–Ti–OH to assemble well on DDA soft templates, leading to more developed mesoporosity of the resulting SE-meso-TON. In contrast, the fairly fast hydrolysis in the sol–gel process reduced the assembly time and thus resulted in less mesoporosity after thermal treatments. Porous TiO_2 with an extremely large SSA had ever been synthesised via sol–gel[26,31] or sonochemical[24] syntheses at low temperature without the carbonization process, where the DDA template was washed out before subsequent calcinations. The SSA of those TiO_2 materials declined dramatically due to structural collapse during calcination greater than 300 °C.[24,26,31] Hence, the in situ generated carbon "hard templates" help to preserve the high SSA and developed porosity of the resulting meso-TON during thermal nitriding, removal of the template and crystallization.

Fig. 4 compares the UV-vis diffuse reflectance spectra of the P25 TiO_2 and the meso-TON materials calcined at 450 °C. The SG-meso-TON can absorb more visible light but less UV than SE-meso-TON. The adsorption edges of the SG-meso-TON and SE-meso-TON photocatalysts tailed to 650 and 550 nm,
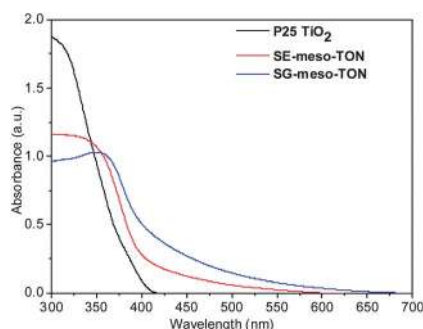

Fig. 4 UV-vis spectra of the SE-meso-TON and SG-meso-TON calcined at 450 °C.

respectively, which is typically characteristic of impurity induced red-shifts.[3,9] Light absorption features of the meso-TON samples suggest that nitrogen was incorporated into the TiO_2 matrix and altered their energy bands.[2,3,27] Applying the Kubelka–Munk function to the diffusion reflectance spectra, the calculated bandgaps of SE-meso-TON and SG-meso-TON are 2.98 and 2.9 eV, respectively, which are much smaller than that of Degussa P25 (3.2 eV). The reduced bandgap energy of the meso-TON gave rise to the midgap states arising from the N-dopants.

The surface composition of the TON materials was determined by X-ray Photoelectron Spectroscopy (XPS). Fig. 5A compares the core lines of N 1s in the meso-TON materials and Degussa P25. No N 1s peaks are observed in Degussa P25, while broad and strong N 1s spectra are clearly observed on the meso-TON materials. The stronger N 1s peak of SG-meso-TON suggests that it contains a higher N-doping level than SE-meso-TON, and the concentrations of the nitrogen dopants were approximately 0.33 atm% and 0.5 atm% for SE-meso-TON and SG-meso-TON, respectively. Asahi et al.[2] claimed that the substitutional N (N_s) with BE at 396 eV in TON materials was more effective for the bandgap narrowing of TiO_2. The N_s can be ruled out since no XPS signals displayed around 396 eV in the N 1s spectra of our meso-TON materials. However, broad N 1s peaks appear within 397–402.5 eV for the meso-TON materials, which can be attributed to different nitrogen species, such as substitutional NO_x (Ti–(NO)$_x$, 398.7–399.5 eV) and interstitial NO_x (398.2–398.5 eV and 400–402 eV).[16,32] Such broad N 1s XPS spectra due to various NO_x-dopants have ever been observed in the N-doped TiO_2.[5,33]

The major O 1s core level appears around 530 eV as shown in Fig. 5B, while broadening of O 1s at 531 eV can be clearly observed which was previously attributed to the presence of the N–Ti–O and O–N–Ti–O bond.[13,16,33] The broadening of O 1s spectra in 531–532.5 eV may be assigned to the surface hydroxyl groups on titania. The three samples are of very similar C 1s XPS spectra centred at 285 eV (Fig. 5C) due to adventitious carbon.[34] This ruled out the doped carbon species in the meso-TON materials.

Fig. 5D shows the Ti 2p spectra of the meso-TON and P25 photocatalysts, where the binding energy (BE) around 464.1–464.6 eV and 458.4–458.9 eV may be assigned to Ti 2p$_{1/2}$ and Ti 2p$_{3/2}$, respectively. In comparison to P25, the Ti 2p spectra of meso-TON materials slightly shifted to higher BE depending on the N concentration: the higher the N-doping level the larger the blue shift. It was reported that the BE shift of Ti 2p XPS highly related to the nature of the N species exists in TON materials.[35] For the N-substituted TiO_2, its Ti 2p XPS would shift (red) to lower BE because of the increased electron density on the Ti cation ($Ti^{4+} \rightarrow Ti^{3+\delta}$) bonded with the substitutional N (N_s). Such an increased electron density results from the lower electronegativity of the N_s in O–Ti–N than O in O–Ti–O bonds.[36] The N_s is of the negative oxidation state and shares the charges with adjacent oxygen vacancies ($V_o^{\cdot}$), which partly reduces the oxidation state of Ti in the O–Ti–N bonds to be $Ti^{3+\delta}$ ($\delta < 1$). It was reported that the Ti 2p XPS peak of $Ti^{3+\delta}$ centres at about 456.2 eV,[3,16] however such a peak was absent in our cases,
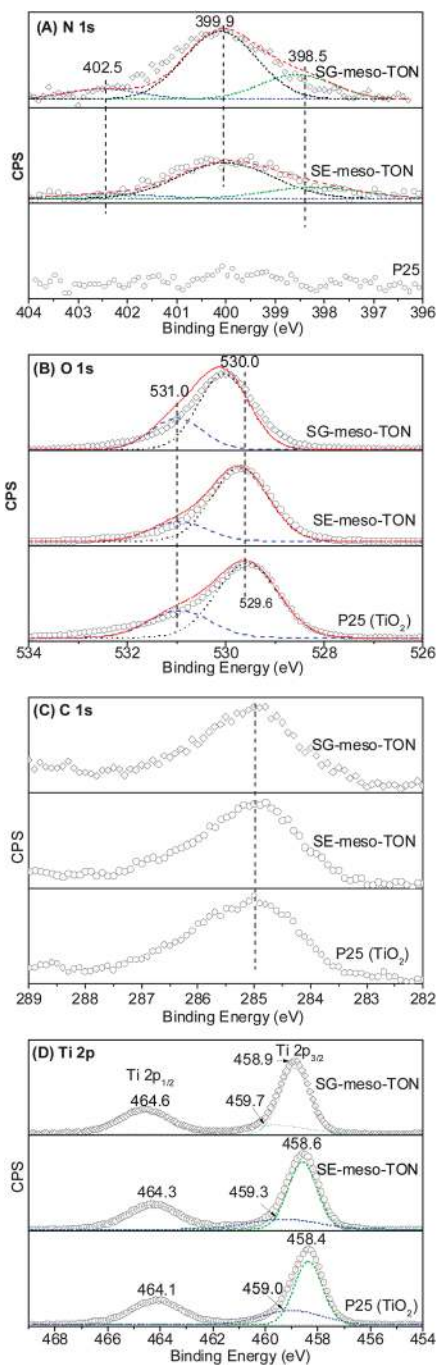
Fig. 5 XPS spectra of TON: (A) N 1s (B) O 1s (C) C 1s and (D) Ti 2p XPS.

Fig. 6 ESR spectra of the meso-TON samples calcined at 450 °C.

indicating that there is no N_s species in our meso-TON materials. In the TON samples with interstitial N-dopants, the N species (N_i) species may be NO or NO_2 or both and such species are of positive oxidation states,[37] corresponding to higher N 1s binding energy in XPS which might incur a slight blue shift of Ti 2p XPS. If the O atom was replaced with a NO_x molecule at the substitutional sites, denoted as $(NO_x)_s$, the Ti 2p XPS should be very similar to those interstitial NO_x species in TON. Therefore, the slight blue-shifts of Ti 2p XPS, shown in Fig. 5D, suggest N species in the meso-TON materials are $(NO_x)_s$ or $(NO_x)_i$ rather than the N_s. Although surface O/Ti atomic ratios of the meso-
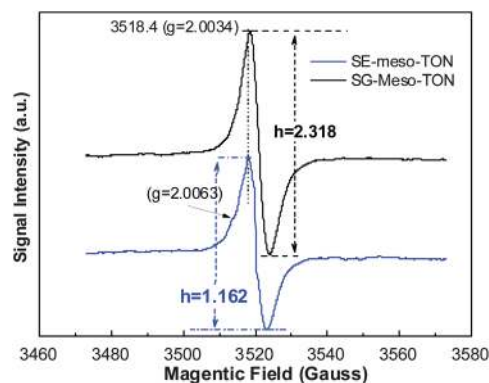
TON are greater than 2, it cannot rule out the existence of $V_o^{\cdot}$ because excess oxygen species may arise from the adventitious carbon or interstitial NO_x species.[38]

Electron spin resonance spectroscopy (ESR) is a most sensitive and accurate technique to detect paramagnetic centers (N-dopants or oxygen vacancies).[16,39] The principal rhombic ESR signals (Fig. 6) of SE-meso-TON and SG-meso-TON are very similar, and their characteristic g tensors at approximately 2.0034 can be assigned to the single-electron-trapped oxygen vacancies $(V_o^{\cdot})$,[40] which is induced by N_i (e.g. NO_x) in the microenvironment either as $Ti(IV) - NO_x - V_o^{\cdot}$ or $Ti(IV) - V_o^{\cdot} - NO_x$.[39,41] No triplet-electron-trapped Ti^{3+} ($g = 1.96$) was observed, which is in good agreement with XPS analysis.[40] Ti^{3+} may be excluded since the samples were prepared in stationary air, an oxidation atmosphere, while the $Ti^{4+} - V_o^{\cdot}$ is energetically more favorable, according to the DFT calculations.[42–44] By comparing the major ESR intensity ($h_{SE}/h_{SG} = 2.318/1.162$) of SG-meso-TON and SE-meso-TON samples, the relative concentration of the $V_o^{\cdot}$ is at a ratio of approximately 2.0.[16,41] The larger amount of $V_o^{\cdot}$ in SG-meso-TON is related to its higher N-doping level than SE-meso-TON.

In comparison to the major ESR signals in Fig. 6, the signals with respect to adsorbed NO_x species,[39,41] g tensors around both 2.027 and 1.98, are very weak. This is in good agreement with the previous reports that the paramagnetic NO_x species in the N-doped TiO_2 cannot be detectable by X-band ESR at room temperature.[42] The ESR characterizations are also experimentally in agreement with XPS characterizations, the N-species in the TON should be NO_x connected directly ($Ti - NO_x - V_o^{\cdot}$, substitutional NO_x) or indirectly ($Ti - V_o^{\cdot} - NO_x$) to Ti^{4+}. The interstitial NO_x prefers to adsorb on oxygen vacancies,[3,9] while the substitutional NO_x favours the formation of oxygen vacancies.[16,32]

Despite the nature and sites of doped NO_x species, they can lead to formation of a midgap state, just above the top of TiO_2 VB, which mainly comprises of O 2p states. Meanwhile, the $V_o^{\cdot}$ will lead to another midgap which is energetically under CB of TiO_2, comprising the 3d state of Ti^{4+} ions.[43] On the basis of the above discussions, the bandgap structures of the meso-TON and TiO_2 are comparatively illustrated in Scheme 1. It clearly reveals that the narrowing of the bandgap of TON materials is a synergetic result of the doped NO_x species and $V_o^{\cdot}$, and is responsible for the visible light response.
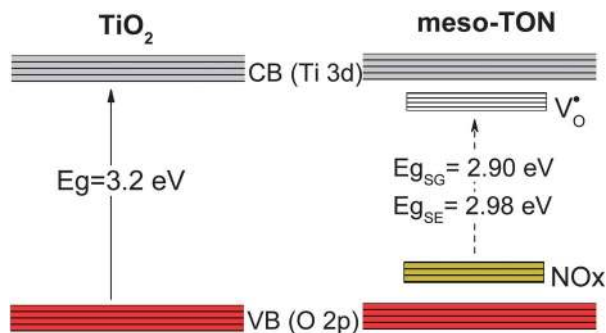
Scheme 1 The schematic bandgap structures of TiO$_2$ and TON.

Fig. 7A shows the visible-light-induced photodegradation of refractory organic dye, RhB, as a function of the irradiation time. The SE-meso-TON sample can completely degrade RhB in 30 minutes, while only 50% RhB could be degraded on the SG-meso-TON in 30 minutes under the same reaction conditions (1.0 g L^{-1} photocatalyst, 10 ppm RhB, neutral pH, and room temperature). The photodegradation of 30% RhB on TiO$_2$ Degussa P-25 may be attributed to both the dye-sensitizing effect and its rutile component since the rutile component may also harvest a little visible light due to its smaller bandgap.[45] Fig. 7B presents the first order reaction kinetics plots of RhB photodegradation on the meso-TON samples. From Fig. 7B, the apparent reaction kinetics constant k, can be extracted from the slope of the plot of ln(c/c_0) vs. reaction time, where c and c_0 represent the current and initial concentration of the RhB solution, respectively. The calculated k values are listed
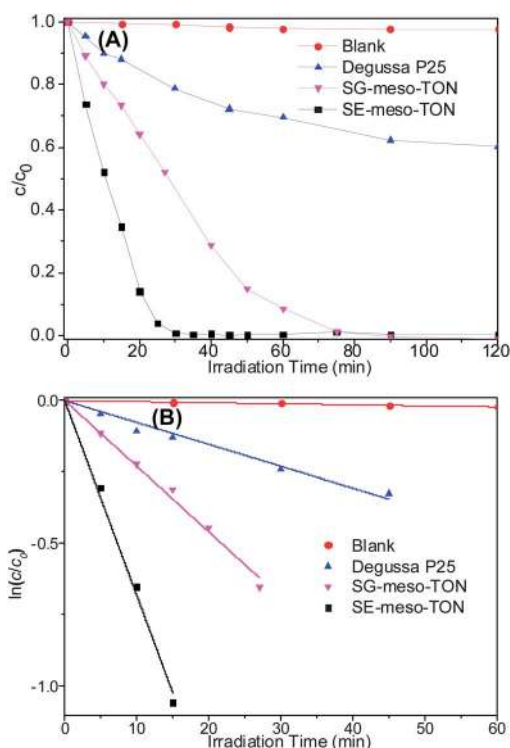
in Table 1. It can be seen that k of SE-meso-TON is 3.0-fold (=$k_{SE-meso-TON}/k_{SG-meso-TON}$) of SG-meso-TON.

Table 1 also includes the so-called turnover frequency (TOF), which is defined as the ratio of the reaction rate constant to the surface areas per unit time, reflecting the intrinsic reaction activity of the photocatalyst.[37] Although the surface area of SE-meso-TON is nearly twice of SG-meso-TON, it can be seen that the TOF on SE-meso-TON is 1.63 times to that on SG-meso-TON, a little lower than the apparent relative activity ($k_{SE-meso-TON}/k_{SG-meso-TON}$), suggesting that the large SSA is not the only factor that contributes to the visible-light-driven photocatalytic activity. Nevertheless, both the results of TOF per unit surface area and reaction rate constants clearly indicate that SE-meso-TON is more active than SG-meso-TON in photodegradation of RhB under visible-light irradiation.

Once we normalize the TOF values with respect to the relative concentration of the oxygen vacancies ($V_o^{.}$, see the discussion in the ESR section), the TOF ratio of SE-meso-TON to SG-meso-TON increased dramatically, approaching to 3.26, very close to the apparent relative activity value, 3.0 ($k_{SE-meso-TON}/k_{SG-meso-TON}$). Such a great increase of the relative specific TOF suggests that $V_o^{.}$ deteriorated the intrinsic activity of SG-meso-TON, which has more $V_o^{.}$ than SE-meso-TON.

It was reported that low N-doping level can facilitate photocatalysis yet higher N-doping level leads to lower photoactivity due to significant recombination of photogenerated charge carriers on the oxygen vacancies caused by excess N-dopants.[46] The suitable levels of N-doping as well as the $V_o^{.}$ concentration offer the enhanced visible-light photoactivity. Therefore, the superior photo-activity of SE-meso-TON to SG-meso-TON can be well associated with its lower $V_o^{.}$ level, larger surface areas and developed porosity. Such developed porosity provides more surface active sites for the adsorption of reactants and desorption of reaction products on the photocatalysts, while the suitable levels of N-dopants and $V_o^{.}$ ensure that the surface active sites are effective and hinder the recombination of photogenerated electrons and holes in photocatalytic reaction.

Conclusion

We developed a simple solvent evaporation induced self-assembly (SEISA) strategy using a single complex precursor to synthesize mesoporous nanocrystalline N-doped TiO$_2$ (SE-meso-TON) with a hierarchical porous structure. Upon calcinations at 450 °C for 4 hours, the SE-TON retained finite crystallite size, mesoporous architecture and large surface area (BET SSA = 101 m^2 g^{-1}) which is nearly twice that of the TON synthesized via a sol–gel route. The SE-meso-TON had strong absorption of visible light up to 550 nm as a result of the doped NO$_x$ species and doping-induced oxygen vacancies. The obtained meso-TON exhibited superb photocatalytic activity in clean-up of RhB dye under visible light irradiation, and the superior visible-light-responsive photoactivity of the SE-meso-TON to SG-meso-TON arose from both the suitable N-doping level and the developed mesoporous texture. XPS spectra revealed that there are several N-dopants existing in the meso-TON which are responsible for the enhanced response to visible

Fig. 7 Visible-light-driven photodegradation of RhB (A) and reaction kinetics (B) on the meso-TON and TiO$_2$ catalysts.

light, while the oxygen vacancy induced by excess N-doping decreases the intrinsic photocatalytic activity of the meso-TON materials.

Acknowledgements

Notes and references

1 S. Sato, *Chem. Phys. Lett.*, 1986, **123**, 126–128.
2 R. Asahi, T. Morikawa, T. Ohwaki, K. Aoki and Y. Taga, *Science*, 2001, **293**, 269.
3 J. Zhang, Y. Wu, M. Xing, S. A. K. Leghari and S. Sajjad, *Energy Environ. Sci.*, 2010, **3**, 715.
4 S. S. Soni, M. J. Henderson, J.-F. Bardeau and A. Gibaud, *Adv. Mater.*, 2008, **20**, 1493.
5 X. Chen, Y. B. Lou, A. C. S. Samia, C. Burda and J. L. Gole, *Adv. Funct. Mater.*, 2005, **15**, 41.
6 W. Guo, Y. Shen, L. Wu, Y. Gao and T. Ma, *J. Phys. Chem. C*, 2011, **115**, 21494.
7 J. Wang, B. Mao, J. L. Gole and C. Burda, *Nanoscale*, 2010, **2**, 2257.
8 W. Zhang, L. D. Zou and L. Z. Wang, *Water Sci. Technol.*, 2010, **61**, 2863.
9 H. Choi, M. G. Antoniou, M. Pelaez, A. A. delaCruz, J. A. Shoemaker and D. D. Dionysiou, *Environ. Sci. Technol.*, 2007, **41**, 7530.
10 Z. Jiang, F. Al-Shahrani, T.-W. Lin, Y. Cui and T. Xiao, *Stud. Surf. Sci. Catal.*, 2007, **165**, 355.
11 G. Liu, Y. Zhao, C. Sun, F. Li, G. Lu and H.-M. Cheng, *Angew. Chem., Int. Ed.*, 2008, **47**, 4516.
12 E. Martínez-Ferrero, Y. Sakatani, C. Boissière, D. Grosso, A. Fuertes, J. Fraxedas and C. Sanchez, *Adv. Funct. Mater.*, 2007, **17**, 3348.
13 Z. Jiang, F. Yang, N. Luo, B. T. T. Chu, D. Sun, H. Shi, T. Xiao and P. P. Edwards, *Chem. Commun.*, 2008, 6372.
14 J. Ma, L. S. Qiang, X. B. Tang and D. Y. Tang, *Chin. J. Inorg. Chem.*, 2010, **26**, 963.
15 B. Chi, L. Zhao and T. Jin, *J. Phys. Chem. C*, 2007, **111**, 6189.
16 F. Zou, Z. Jiang, X. Qin, Y. Zhao, L. Jiang, J. Zhi, T. Xiao and P. P. Edwards, *Chem. Commun.*, 2012, **48**, 8514.
17 J. Yuan, M. Chen, J. Shi and W. Shangguan, *Int. J. Hydrogen Energy*, 2006, **31**, 1326.
18 M. Gohin, I. Maurin, T. Gacoin and J.-P. Boilot, *J. Mater. Chem.*, 2010, **20**, 8070.
19 S. Yin, Y. Aita, M. Komatsu, J. Wang, Q. Tang and T. Sato, *J. Mater. Chem.*, 2005, **15**, 674.
20 J. A. Rengifo-Herrera, E. Mielczarski, J. Mielczarski, N. C. Castillo, J. Kiwi and C. Pulgarin, *Appl. Catal., B*, 2008, **84**, 448.
21 T. Xiao, Z. Jiang, *WO Pat.*, 2008009919, 2008.
22 J.-G. Li and T. Ishigaki, *Acta Mater.*, 2004, **52**, 5143.
23 H. Zhang and J. F. Banfield, *J. Phys. Chem. B*, 2000, **104**, 3481.
24 Y. Wang, X. Tang, L. Yin, W. Huang, Y. R. Hacohen and A. Gedanken, *Adv. Mater.*, 2000, **12**, 1183–1186.
25 Z.-Y. Yuan, T. Z. Ren and B. L. Su, *Adv. Mater.*, 2003, **15**, 1462.
26 D. M. Antonelli, *Microporous Mesoporous Mater.*, 1999, **30**, 315.
27 T. Ma, M. Akiyama, E. Abe and I. Imai, *Nano Lett.*, 2005, **5**, 2543.
28 J. G. Yu, Y. R. Su and B. Cheng, *Adv. Funct. Mater.*, 2007, **17**, 1984.
29 K. S. W. Sing, D. H. Everett, R. A. W. Haul, L. Moscou, R. A. Pierotti, J. Rouquérol and T. Siemieniewska, *Pure Appl. Chem.*, 1985, **57**, 603.
30 G. Yang, Z. Jiang, H. Shi, T. Xiao and Z. Yan, *J. Mater. Chem.*, 2010, **20**, 5301.
31 D. M. Antonelli and J. Y. Ying, *Angew. Chem., Int. Ed.*, 1995, **34**, 2014.
32 S.-H. Lee, E. Yamasue, K. N. Ishihara and H. Okumura, *Appl. Catal., B*, 2010, **93**, 217.
33 J. H. Pan, G. Han, R. Zhou and X. S. Zhao, *Chem. Commun.*, 2011, **47**, 6942.
34 J. Fang, F. Wang, K. Qian, H. Bao, Z. Jiang and W. Huang, *J. Phys. Chem. C*, 2008, **112**, 18150.
35 F. Zuo, L. Wang, T. Wu, Z. Zhang, D. Borchardt and P. Feng, *J. Am. Chem. Soc.*, 2010, **132**, 11856.
36 M. Sathish, B. Viswanathan, R. P. Viswanath and C. S. Gopinath, *Chem. Mater.*, 2005, **17**, 6349.
37 B. Viswanathan and K. R. Krishanmurthy, *Int. J. Photoenergy*, 2012, **2012**, 10.
38 Q. Sun and Y. Xu, *J. Phys. Chem. C*, 2010, **114**, 18911.
39 C. Feng, Y. Wang, Z. Jin, J. Zhang, S. Zhang, Z. Wu and Z. Zhang, *New J. Chem.*, 2008, **32**, 1038.
40 Y. Wang, C. Feng, M. Zhang, J. Yang and Z. Zhang, *Appl. Catal., B*, 2011, **104**, 268.
41 Y. Wang, C. Feng, M. Zhang, J. Yang and Z. Zhang, *Appl. Catal., B*, 2010, **100**, 84.
42 C. Di Valentin, G. Pacchioni, A. Selloni, S. Livraghi and E. Giamello, *J. Phys. Chem. B*, 2005, **109**, 11414.
43 C. Di Valentin, E. Finazzi, G. Pacchioni, A. Selloni, S. Livraghi, M. C. Paganini and E. Giamello, *Chem. Phys.*, 2007, **339**, 44.
44 C. Di Valentin, E. Finazzi, G. Pacchioni, A. Selloni, S. Livraghi, A. M. Czoska, M. C. Paganini and E. Giamello, *Chem. Mater.*, 2008, **20**, 3706.
45 H. Xu, Z. Zheng, L. Zhang, H. Zhang and F. Deng, *J. Solid State Chem.*, 2008, **181**, 2516.
46 K. Yang, Y. Dai and B. Huang, *J. Phys. Chem. C*, 2007, **111**, 12086.